



Energy dissipation in horizontally driven particle dampers of low acceleration intensities

Niklas Meyer · Robert Seifried

Received: 16 June 2021 / Accepted: 7 March 2022 / Published online: 16 March 2022
© The Author(s) 2022

Abstract The energy dissipation in sinusoidally driven particle dampers is highly dependent on the motion mode of the particle bed. Especially, for applications of low acceleration intensity, i.e., acceleration amplitude below gravitational acceleration, only small energy dissipation rates are obtained so far, due to sticking of particles. Here, a new and more efficient design of particle dampers is introduced for such applications, whereby the focus is on horizontal vibrations. The proposed design makes use of the rolling property of spheres inside particle containers with flat bases. First, a cuboid container shape is studied. Two different motion modes are observed experimentally within this container shape. For low driving amplitudes, the particle bed is showing a scattered behavior resulting in a low damping efficiency. For high driving amplitudes instead, the rolling collect-and-collide state is observed resulting in much higher efficiency. Analytical descriptions for the energy dissipation are derived for both motion modes, being in good agreement with experimental measurements. It is obtained that the optimal working point of such dampers, i.e., the optimal stroke, is only depending on the filling ratio of the damper. Additionally, the optimal working point separates both motion modes. For lower strokes as the optimal one, the scattered state is observed, while for higher

strokes the rolling collect-and-collide mode is seen. Sensitivity analyses are performed using the experimental setup and discrete element simulations. It is obtained that especially a low friction coefficient and a high particle radius are beneficial. On the other hand, a small tilt around the container's longitudinal or pitch axis might significantly decrease the efficiency of the damper. Besides the cuboid container, the effect of a cylindrical container heading against gravity is analyzed. While the particle bed motion modes are only little influenced, the efficiency of the damper becomes independent of the excitation direction in the horizontal plane. Thus, such dampers could be applied to a large field of applications in mechanical and civil engineering.

Keywords Particle damper · Rolling bed · Horizontal vibrations · Granular material · Complex power method

1 Introduction

Subjecting a container partially filled with granular material with a harmonic motion, a variety of different motion modes of the particle bed have been observed by multiple authors, e.g., [30, 31, 36, 37]. These motion modes depend on specific particle properties and operation conditions, like particle size, excitation direction and intensity, or gravity. An important property of each

N. Meyer (✉) · R. Seifried
Institute of Mechanics and Ocean Engineering, Hamburg
University of Technology, Eißendorfer Straße 42, Hamburg
21073, Germany
e-mail: n.meyer@tuhh.de

motion mode is the energy dissipation inside the moving granular material, which may vary a lot.

Applications of such containers filled with granular material are particle dampers. They are used to reduce structural vibrations and are becoming more and more popular. Hereby, the granular containers are attached to the vibrating structure. By structural vibrations, momentum is transferred to the granular material which interacts with each other. As a result, energy is dissipated by impacts and frictional phenomena between the particles.

Particle dampers are cost-efficient devices, add only little mass to the primary system [14], and might be applied to a wide frequency range [5]. Furthermore, they are robust against harsh environmental conditions [28,33], like in spacecraft applications [27]. Although particle dampers show huge potential, their design is still a challenging task. This is because motion modes and energy dissipation correlate in a non-trivial way, which is often poorly understood. Identifying these correlations is still part of ongoing research, see [2,7,8,18,19,31,34,36,38].

By Mehta and Luck [21], the completely inelastic bouncing ball was studied. Inspired by this, recently, an analytical equation for the energy dissipation of the bouncing collect-and-collide motion mode was derived by Bannerman et al. [3] and Sack et al. [30] under the condition of weightlessness, i.e., in the absence of gravity. In this motion mode, the particles move as one single particle block, colliding inelastically with the container walls. Bannerman et al. [3] and Sack et al. [30] obtain that the center of mass of the particles moves synchronously with the driven particle container. To validate their analytical predictions, their experiments were performed during parabolic flights. While Sack et al. [30] subjected their particle container to a harmonic motion via a linear drive, Bannerman et al. [3] mounted their damper at the tip of a simple beam-like structure. Either way, they found a good agreement between their analytical equation and their experimental results. Finally, they conducted that the optimal working point of the bouncing collect-and-collide motion mode is only depending on the filling ratio of the damper but not on the excitation frequency. In [23], it is shown that their analytical formula is even still valid under the effect of gravity for horizontal and vertical vibrations and high acceleration intensities.

However, for applications of low acceleration intensities, i.e., acceleration amplitude below gravitational

acceleration, and under the effect of gravity, the formula of Bannerman et al. [3] and Sack et al. [30] is losing validity. This is because particles begin to stick and no synchronous motion with the particle container is seen anymore [17]. To overcome this problem, the rolling attribute of spheres can be used [4,13,16]. Instead of sticking, the particles slide and roll over the container base. In this paper, the spheres rolling attribute is used within flat container bases for applications of low acceleration intensities. Hereby, the focus is on horizontal excitations, i.e., perpendicular to gravity. Hence, a synchronous particle motion with the driven container is achieved.

At first, a cuboid container shape is studied experimentally and numerically using the discrete element method (DEM). Two different motion modes are observed within this container shape, i.e., the scattered and rolling collect-and-collide motion mode. For low driving amplitudes, the scattered state is seen, while for high driving amplitudes the rolling collect-and-collide motion mode is obtained. The highest damper efficiency occurs at the transition between both motion modes, i.e., at the optimal stroke. It turns out that this optimal stroke is only depending on the filling ratio of the damper. Also, analytical descriptions for the energy dissipation for both motion modes are derived as well as for the optimal stroke.

Sensitivity analyses are performed using the experimental setup and discrete element simulations. Multiple particle properties, like Young's modulus, density, coefficient of restitution (COR), friction coefficient, particle radius, or particle number, are studied. Also, the effect of a tilt around the container's axis is investigated. Besides the cuboid container shape, the effect of a cylindrical container shape which axis oriented in direction of gravity is finally analyzed.

This paper is organized in the following way: In Sects. 2 and 3, the experimental setup and numerical model are introduced to analyze the motion modes and energy dissipation inside the particle container. Their results are given in Sect. 4. In the following Sect. 5, analytical equations for the energy dissipation of the scattered and rolling collect-and-collide motion mode are derived and compared to the experimental measurements and numerical simulations. Further influence parameters on the energy dissipation are investigated by sensitivity analyses in Sect. 6. Finally, the conclusion is given in Sect. 7.

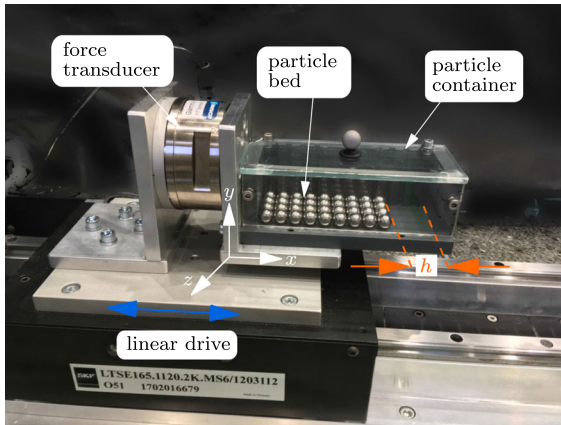


Fig. 1 Experimental setup to analyze motion modes and energy dissipation of the driven particle bed

2 Experimental setup

The main idea of the new damper design is to use the rolling attribute of spheres to obtain a high damper efficiency for low acceleration intensity vibrations. In contrast to the design of other authors, e.g., [3, 10], a particle container with a cuboid shape and spherical particles is used. By only using one layer of particles, the particles roll and slide over the container base instead of sticking together.

The experimental setup to analyze the particle bed motion modes and energy dissipation under horizontal forced vibration is shown in Fig. 1. It consists of a cuboid particle container mounted via a force transducer on a linear drive. Thus, the excitation force acting on the particle container is measured. The particle container is made of polyvinyl chloride (PVC) and has a quadratic cross section with an inner edge width w and height h of 40 mm and a length L of 120 mm in excitation direction. The container is filled with steel (S235) spheres of $r = 5$ mm radius throughout this paper. As these spheres are also used for ball bearings in the hardened form, they have a high degree of roundness. To reduce friction, the particles are lubricated with a little bit oil. Between particle container and linear drive, the force transducer GAMMA- - SI- 32- - 2.5 from company SCHUNK is mounted to measure the excitation force. The linear drive is from SKF and SIEMENS, named LTSE 165. Its position is measured by the incremental encoder LIA20 of NUMERIC JENA with a resolution of $20\ \mu\text{m}$. The control of the linear drive is done by the motion controller SIMOTION

D435–2 of SIEMENS and the SINAMICS variable-speed drive with a sampling frequency of 8 kHz. Thus, this setting ensures accurate control and fast reaction on safety issues. For further details, see [25, 26]. The measured results, which are the container motion and the driving force acting on the container, are saved with a sampling frequency of 1 kHz for later post-processing.

In the experiments, the linear drive excites the particle container sinusoidally as $x_c = X \sin(\Omega t)$, with the container amplitude X and angular frequency $\Omega = 2\pi f$. The corresponding container velocity and acceleration follow as $\dot{x}_c = V \cos(\Omega t)$ and $\ddot{x}_c = -A \sin(\Omega t)$ with $V = X\Omega$ and $A = X\Omega^2$. To analyze the different effects and influence parameters, the excitation amplitude varies between $X = 0.5$ mm till $X = 50$ mm using 40 sample points and a logarithmic distribution. The excitation frequency is set exemplary to $f = 2$ Hz. Indeed, it turns out that there exist a lower and upper limit for the excitation frequency, which is discussed later. Each sample point is measured for 20 vibration cycles. After measuring each sample point, the linear drive pauses, so the particles can come to rest. As only the stationary state of the system shall be analyzed, during post-processing the first two vibration cycles are cut off to remove the irregular movement of the particles thru their initial state.

3 Numerical model

To study the particle damper numerically, the discrete element method (DEM) [6] is used. It is a discrete simulation method for granular materials. Every particle is considered as an unconstrained moving body only influenced by applied forces. The dynamics are described by Newton's and Euler's equation of motion for every particle [29] and are mainly influenced by contacts between particles themselves and walls. To model a contact, the contact partners are treated as rigid, thus contact occurs only at a single point. This contact modeling allows the contact partners to overlap continuously. The overlap δ is counteracted by the resulting contact forces.

In this research, the algorithms presented in [22] are used. For the contact search, the verlet list in combination with the link cell algorithm is applied. The formula of Gonthier [11] is used for the normal contact forces

and reads

$$F_N = k\delta^{3/2} (1 + d\delta). \quad (1)$$

It is based on the contact law of Hertz [12] using physical parameters of the contact partners to describe the contact stiffness k , namely the particle radius r , the Young's modulus E , and the Poisson's ratio ν . The nonlinear damping parameter d depends mainly on the coefficient of restitution (COR) ε , which controls the amount of energy dissipation during the contact. For $\varepsilon = 1$, the contact procedure is fully elastic, while for $\varepsilon = 0$, the contact procedure is fully inelastic. In DEM simulations, often a constant COR value is used. Indeed, this is in reality not the case, as the COR shows a high dependency on impact velocity, which can be determined experimentally or numerically using the finite element method [23,24]. For the tangential forces, sliding friction with friction coefficient μ using a smoothing hyperbolic tangent function to avoid jumps in the friction forces at zero velocity [1] is utilized, reading

$$F_R = -\mu |F_N| \tanh(\tau |v_p^t|), \quad (2)$$

with v_p^t being the relative, tangential velocity at the contact point P and τ the smoothing parameter. The friction coefficient is set to 0.1 for all contacts [24]. The time integration is performed using a variable time step fifth-order Gear predictor–corrector algorithm [9].

For the numerical analysis, the same excitation and post-processing parameters as in the experiments are chosen, see Sect. 2. The used material and contact data are listed in Table 1. Although the experimental testbed is set up very precisely, still little manufacturing and mounting inaccuracies exist. Especially, the container width is slightly higher with a value of about

40.4 mm. Also, little tilts around the container axis are observed using a spirit level. To account for these little tilts, a tilt of 0.1° around all container axis is used for the simulations if not stated differently. It should be noted that these adjustments seem to be of minor importance. However, neglecting these inaccuracies can lead to abnormal or unrealistic behavior in the simulations.

4 Experimental and numerical results

In this section, the experimental and numerical results of the previously introduced models are presented. For the data analysis the complex power method, introduced in Sect. 4.1, is used. The results are then presented in the following Sect. 4.2.

4.1 Complex power

To analyze the energy dissipation and the efficiency of the particle damper, the complex power method, introduced by Yang [35], is used. The complex power is determined to

$$P = \frac{1}{2} F^{*\top} \bar{V}^*. \quad (3)$$

Hereby, F^* denotes the complex amplitude calculated by the fast Fourier transform (FFT) of the driving force signal acting on the container and \bar{V}^* is the conjugate complex amplitude by FFT of the velocity signal of the container motion. The dissipated energy per cycle \tilde{E}_{diss} follows from the complex power to

$$\tilde{E}_{\text{diss}} = 2\pi E_{\text{diss}} = \frac{2\pi}{\Omega} \text{Real}(P). \quad (4)$$

Table 1 Material parameters of spheres and container

Material	Sphere S235	Container PVC
Young's modulus [GPa]	208	3
Poisson's ratio [-]	0.3	0.38
Density [kg/m ³]	7900	1400
Friction coefficient [-]	0.1 for all contacts	
Coefficient of restitution [-]	Velocity dependent, see [23,24]	
Dimensions	$r = 5 \text{ mm}$	$L, w, h = 120, 40.4, 40.0 \text{ mm}$

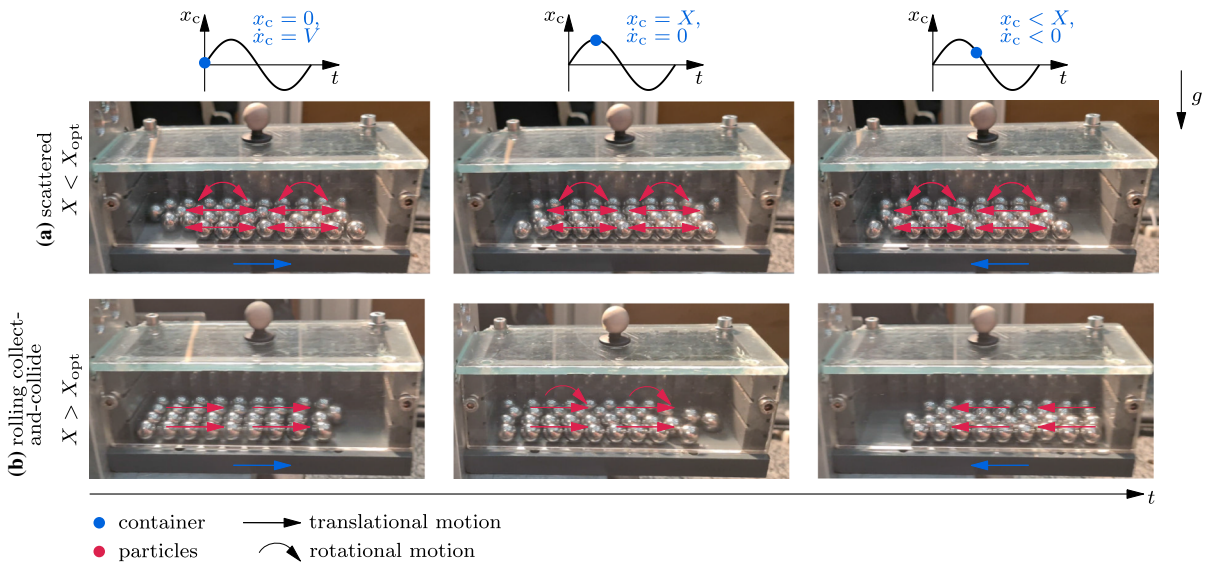


Fig. 2 Observed motion modes at different container strokes. Top: Scattered state. Bottom: Rolling collect-and-collide

To judge the damper’s efficiency the reduced loss factor η^* [18,23] is used. It is calculated by a scaling of the dissipated energy with the kinetic energy of the particle system E_{kin} using the mass of the particle bed m_{bed} , i.e., the mass of all particles, to

$$\eta^* = \frac{E_{diss}}{E_{kin}} = \frac{E_{diss}}{\frac{1}{2}m_{bed}|V_{\Omega}^*|^2}, \tag{5}$$

with V_{Ω}^* being the complex amplitude by FFT of the velocity signal at the driving frequency. As consequence, the reduced loss factor is independent of the container and particle mass and enables the comparison of different particle settings.

4.2 Results

For the experiments, the particle container is filled with $N_p = 36$ and $N_p = 44$ particles, respectively. The maximum particle number necessary to cover the container base with one layer of particles is $N_{p,max} = 48$. The clearance h , i.e., the distance from the particle bed to the opposite container wall, see also Fig. 1, is calculated as

$$h = L \left(1 - \frac{N_p}{N_{p,max}} \right). \tag{6}$$

The clearance is thus calculated to $h_{36} = 30$ mm and $h_{44} = 10$ mm for the two different particle settings.

During all experiments, the particle bed does not take off the container base. Only in rare cases, single particles take off. This happens especially for high container amplitudes. However, after a couple of vibration cycles these flying particles normally sequence again into the particle bed. This happens as the container acceleration amplitude A stays always below the gravitational acceleration $g = 9.81$ m/s². Hence, the gravitational acceleration is the upper bound for the container acceleration and thus for the container stroke and excitation frequency. Increasing the container acceleration amplitude above g the particle bed becomes first in a state of fluidization and turns finally in the bouncing collect-and-collide motion mode. Indeed, the transition between the motion modes is smooth, but these analyses are above the scope of this paper, see [24] for a detailed discussion.

During the conducted experiments, two different motion modes of the particle bed are observed. Snapshot of these motion modes is shown in Fig. 2 for different container positions.

The resulting particle trajectories obtained from DEM simulations are shown in Fig. 3.

For low excitation amplitudes, the system is in the so-called scattering motion mode. Due to friction, almost no particle movement and only few collisions

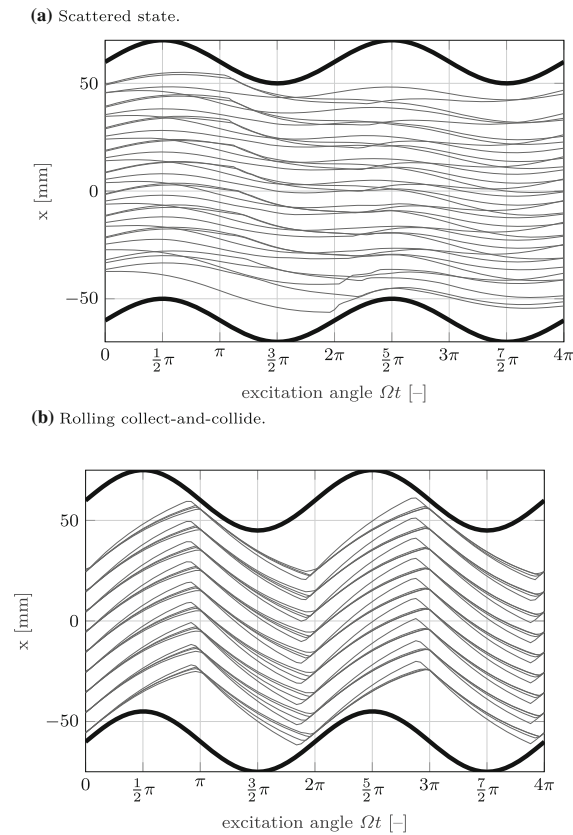


Fig. 3 Particles trajectories obtained from DEM simulations for different container strokes. **a** Scattered state. **b** Rolling collect-and-collide

with the container walls are seen. Hence, no regular or synchronous motion of the particles is obtained, i.e., each particle moves in a different way. When the container amplitude reaches a certain threshold amplitude X_{opt} the system turns suddenly into the rolling collect-and-collide motion mode. Here, the particle bed stays together as one particle block and rolls in the ideal case over the container base. However, the case of ideal rolling might not always hold and thus additional slip occurs. The collisions with the container walls are inelastic, i.e., after impact the particle bed has adopted the container’s velocity and does not rebound from it. This happens due to multiple inter-particle collisions during impact. For further explanations see [3,20,32]. Hence, a synchronous particle motion with the container is achieved. However, for both particle numbers, i.e., for 36 and 44 particles, the container stroke for which the particle system switches its motion mode differs with $X_{opt,36} = 12\text{mm}$ and $X_{opt,44} = 4\text{mm}$.

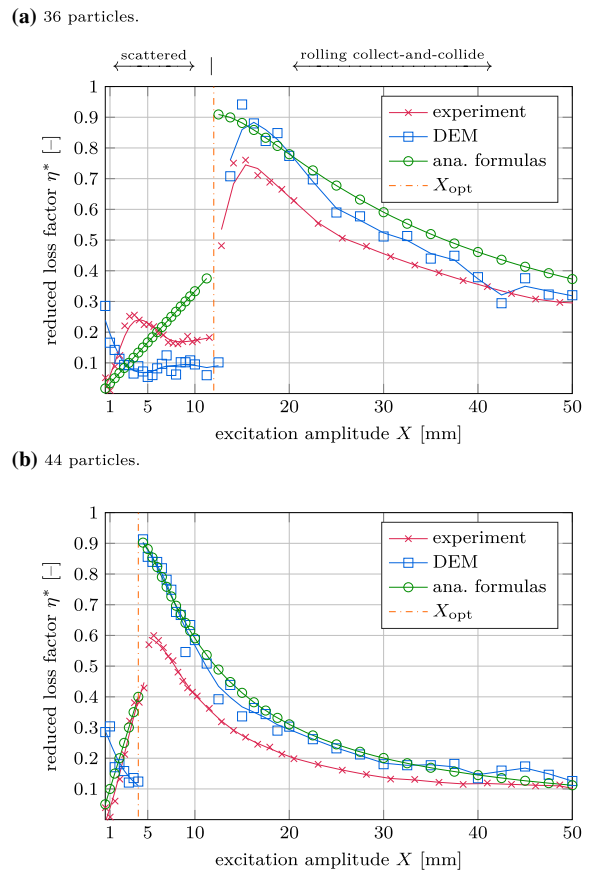


Fig. 4 Reduced loss factor of **a** 36 particles and **b** 44 particles. The threshold amplitude X_{opt} refers to Eq. (17)

It could be expected that within the scattered motion mode, a subharmonic response of the rolling collect-and-collide motion mode might occur. This question has been dealt with for the case of weightlessness by Kollmer [15]. It is found that such a subharmonic response is only theoretically possible for highly inelastic particle collisions (very low COR’s) and is, hence, not observed here.

In Fig. 4, the reduced loss factors of the conducted experiments and numerical analysis are shown. The legend entry “ana. formulas” will be explained later in Sect. 5.

First, the experimental results are discussed. For small excitation amplitudes $X < X_{opt}$, both systems are in the scattered state. Here, only small reduced loss factor values $0 < \eta^* < 0.4$ are obtained. At $X \approx X_{opt}$, both systems switch to the rolling collect-and-collide motion mode. Here, the highest reduced loss factors

are seen, with $\eta_{\max,36}^* = 0.75$ and $\eta_{\max,44}^* = 0.6$. The shape of the reduced loss factor is quite similar for the different particle numbers. The reduced loss factor starts at the high values and reduces slowly to higher excitation amplitudes. However, as X_{opt} is different for both settings, shifted excitation amplitudes are observed.

From these observations, it follows that the rolling collect-and-collide motion mode is of much higher interest for the damper design for an underlying structure as a higher damper efficiency is achieved. Especially, an operation within the maximum reduced loss factors should be aimed. Thus, the rolling collect-and-collide motion mode and its influence parameters are of major interest in this paper.

The numerical DEM results for the reduced loss factor are also pictured in Fig. 4. For the scattered motion mode, i.e., $X < X_{\text{opt}}$, the results are on the same scale as the experimental results. However, neither a qualitative nor quantitative agreement of the observed curves for this area is achieved. As the reduced loss factor and the kinetic energy of the particles are low for this motion mode, very low energy dissipation is achieved in this regime, see Eq. (5). Hence, the energy dissipation of this regime might be very sensitive. This will be further analyzed in Sect. 6. For the rolling collect-and-collide motion mode, i.e., $X > X_{\text{opt}}$, a good qualitative agreement with the experiments is observed. For strokes around the optimal one $X \approx X_{\text{opt}}$, the DEM leads to higher reduced loss factor values compared to the experiments. For the 36 and 44 particle, setting differences up to 0.2 and 0.3, respectively, are obtained. For strokes significantly above the optimal stroke, experimental and numerical results converge against each other for both particle numbers.

5 Analytical description

As seen in Fig. 4, the reduced loss factor and thus, the energy dissipation of the particle bed are strongly related to the two different motion modes. While for the scattered state rather low values are obtained, the rolling collect-and-collide leads especially in the area of X_{opt} to high reduced loss factor values. For both motion modes, an analytical equation shall be found in the following to describe the energy dissipation of the particle bed.

5.1 Scattered state

This motion mode is characterized by its non-regular movement. It is similar to the gas-like state observed by Sack et al. [30] under the condition of weightlessness. Thus, it can be assumed that the dissipated energy is proportional to the number of particle–wall collisions. This collision number depends on the volume swept by the container. As the particles hitting the container walls at random phases, a higher excitation stroke leads to more collisions while a higher clearance to less collisions. Furthermore, the dissipated energy is assumed to scale with the particles kinetic energy. Using an empirical approach to derive an analytical equation for the energy dissipation considering the above-mentioned observations results finally in

$$E_{\text{diss}} = \kappa \frac{X}{h} E_{\text{kin}} = \kappa \frac{X}{h} \frac{1}{2} m_{\text{bed}} V^2, \quad (7)$$

with κ being a scaling factor. For this energy dissipation, the reduced loss factor is then achieved to

$$\eta^* = \kappa \frac{X}{h}, \quad (8)$$

yielding a linear increase with increasing excitation amplitude. Besides the excitation amplitude, Eq. (8) is only further depending on the clearance and thus on the dampers filling ratio. This analytical solution is shown for $\kappa = 1$ in Fig. 4 for $X < X_{\text{opt}}$, i.e., the scattering motion mode. For the 36 particle setting, see Fig. 4a, only a rough approximation is achieved. First, the analytical formula underestimates the reduced loss factor and later on overestimates it. For the 44 particle setting instead, a good quantitative agreement is seen for the whole scattering state, see Fig. 4b. These different matches of experiments and analytical formula can be explained as Eqs. (7) and (8) are derived empirically and not by formulas describing the physical behavior of the motion of the particles. One should also keep in mind that for the scattered state as well the reduced loss factor as the dissipated energy of the particle system are low. Thus, this regime should be avoided for practical applications and an accurate description of the energy dissipation is not of such high practical importance as for the rolling collect-and-collide motion mode.

5.2 Rolling collect-and-collide

From the experiments, it is observed that in the rolling collect-and-collide motion mode, i.e., for $X > X_{\text{opt}}$, the particle bed moves as one single particle block, see Figs. 2 and 3. Thus, the translational and rotational velocities of every single particle are assumed to be identical. It is also observed that the particle bed is first pushed by the container wall. Then, the particle bed leaves the pushing container wall at the container's maximum velocity, i.e., at $\Omega t = n\pi$ with $n \in \mathbb{N}$. At this time point, the container velocity is maximal with $\dot{x}_c = \pm V$. As the particle bed is pushed by the container until, it leaves the container wall, up to this time point almost no rotational movement is seen. Hence, it is assumed to be zero until the particles are leaving the container wall. After leaving the container wall, the particles begin to roll due to friction between particles and container base. Here, a perfect instantaneous transition from sliding to rolling of the particles is assumed. Hence, energy conservation is supposed until the particle bed impacts with the opposite container wall. The conservation of energy balance for a single particle before and after leaving the pushing container wall follows to

$$\frac{1}{2}m_p V^2 = \frac{1}{2}m_p \dot{x}_p^2 + \frac{1}{2}I\dot{\varphi}^2, \quad (9)$$

with \dot{x}_p being the particles absolute translational velocity, m_p and I being the mass and moment of inertia of a single spherical particle, and $\dot{\varphi}$ being the particles angular velocity. Hereby, \dot{x}_p and $\dot{\varphi}$ are assumed to be identical for all particles. To solve for the particles absolute translational velocity \dot{x}_p , the angular particles velocity $\dot{\varphi}$ has to be expressed by it. Using the rolling condition, reading $\dot{\varphi} = (\dot{x}_p - \dot{x}_c)/r$, one obtains

$$\dot{x}_p = \frac{1}{7}V \left(2 \cos(\Omega t) + \sqrt{25 + 10 \sin^2(\Omega t)} \right). \quad (10)$$

The relative velocity between particle bed and container $\Delta\dot{x}_{\text{cp}} = \dot{x}_p - \dot{x}_c$ follows to

$$\Delta\dot{x}_{\text{cp}} = \frac{1}{7}V \left(\sqrt{25 + 10 \sin^2(\Omega t)} - 5 \cos(\Omega t) \right). \quad (11)$$

Interestingly, Eqs. (10) and (11) only depend on the container's velocity amplitude V and the excitation

angle Ωt , but are independent of the particle's properties, like mass or radius.

Next, the particle bed collides with velocity $\dot{x}_p^-(t_i)$ inelastically with the opposite container wall at the impact time point t_i . The impact time point is limited by $\Omega t_i = \pi$. For this time point, the container is again located at $x_c = 0$ but moves in the other direction, i.e., $\dot{x}_c = -V$. If the particle bed hits the container at a later instant of time, the observation that the particle bed leaves the container wall at $x_c = 0$ would be violated for the next vibration cycle. In the experiments, the scattering state is observed instead if the leave condition is violated.

In Fig. 5a, the position of the particle bed and the positions of the pushing (solid line) and impacting (dashed line) container wall normalized by the container position X during the particles rolling phase are shown. As the distance between both container walls depends on the clearance h , the position of the impacting container wall (dashed line) indicates just one possible configuration. It should be noted that for the rolling motion mode the particle impact could occur at any instance of time up to $\Omega t = \pi$ depending on the clearance h . In Fig. 5b, the absolute velocities of the particles \dot{x}_p and relative velocities to the container $\Delta\dot{x}_{\text{cp}}$ normalized by the container velocity V are shown.

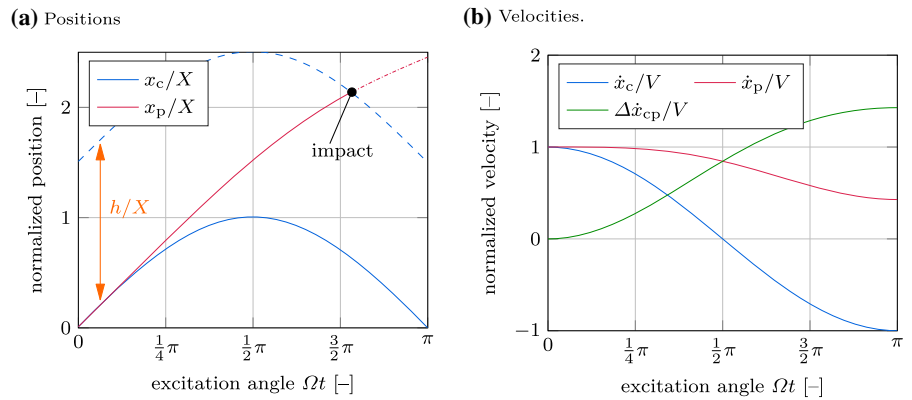
The particles' velocities decrease monotonically until impact due to the rolling condition. However, the relative velocity between particles and container is monotonically increasing. It should be noted that a higher container amplitude X and thus, a higher container velocity V leads to an earlier impact of the particle bed with the opposite container wall, i.e., Ωt decreases. Consequently, the velocity ratio $\Delta\dot{x}_{\text{cp}}/V$ decreases as X increases.

To obtain the particles impact velocity with the opposite container wall $\dot{x}_p^-(t_i)$, the impact time point t_i is necessary. It describes the time the particle bed needs to travel from the pushing to the opposite container wall. It is achieved by solving

$$\underbrace{\int_0^{t_i} \dot{x}_p(t) dt}_{\text{particle motion}} = \underbrace{X \sin(\Omega t_i)}_{\text{container motion}} + \underbrace{h}_{\text{clearance}}. \quad (12)$$

Using Eq. (10), Eq. (12) can now be solved numerically for the impact time point t_i .

Fig. 5 **a** Position of particle bed and positions of pushing (solid line) and impacting (dashed line) container wall normalized by the container amplitude X . The dashed line indicates just one possible configuration. **b** Absolute and relative velocities of the particles normalized by the container velocity V



During the impact of the particle bed with the container wall an inelastic collision occurs. Thus, the particle bed adopts the velocity of the container, i.e., $\dot{x}_p^+(t_i) = \dot{x}_c^+(t_i)$. During this impact, the rotational movement of the particles stops. In sum, two impacts (left wall, right wall) occur during one vibration cycle. Accordingly, the dissipated energy per cycle follows to

$$\tilde{E}_{diss} = 2 \left(\frac{1}{2} m_{bed} \Delta \dot{x}_{cp}^2(t_i) + \frac{1}{2} I_{bed} \dot{\varphi}^2(t_i) \right), \quad (13)$$

with I_{bed} being the sum of the particles' moment of inertia terms.

Using the rolling condition and inserting Eq. (11) into Eq. (13) yields for the dissipated energy per cycle to

$$\tilde{E}_{diss} = \frac{1}{35} m_{bed} V^2 \left(\sqrt{25 + 10 \sin^2(\Omega t_i)} - 5 \cos(\Omega t_i) \right)^2. \quad (14)$$

Finally, the reduced loss factor η^* is obtained by Eq. (5) and $V_{\Omega}^* = V$.

As seen in Fig. 5b, the highest relative velocity and thus, the highest dampers efficiency of the rolling collect-and-collide motion mode are achieved at an impact time point of $\Omega t_i = \pi$, i.e., at the switch point to the scattering state. This has already been observed experimentally, see Fig. 4. By inserting $\Omega t_i = \pi$ into Eq. (14), the maximum dissipated energy per cycle \tilde{E}_{diss}^{max} and the maximum reduced loss factor η_{max}^* are obtained to

$$\tilde{E}_{diss}^{max} = \frac{20}{7} m_{bed} V^2, \quad (15)$$

$$\eta_{max}^* = \frac{20}{7\pi} \approx 0.91. \quad (16)$$

Hence, this theoretical optimal value of the reduced loss factor can be used to judge different dampers and settings about their efficiency.

To obtain the container stroke X for which $\Omega t_i = \pi$ holds true, i.e., the stroke of maximum efficiency, Eq. (12) is solved with Eq. (10) numerically using this impact time point. This yields the optimal stroke as

$$X_{opt} \approx 0.4h. \quad (17)$$

In agreement with the experimental results, see Fig. 4, this optimal stroke is only depending on the clearance h . It is remarkable that no dependency on the excitation frequency Ω exists.

To validate the analytical formula for the dissipated energy Eq. (14), the reduced loss factors and the optimal strokes are compared in Fig. 4 to the conducted experiments for 36 and 44 particles of the rolling collect-and-collide motion mode, i.e., $X > X_{opt}$. The theoretical threshold X_{opt} shows only minor differences to the experimentally observed ones. Also, the curve progression of the reduced loss factor agrees well with the experiments. However, the obtained values are above the experimentally measured ones for all excitation amplitudes. This starts at the optimal strokes with rather high differences of about 0.2 and 0.3 for the 36 and 44 particle settings, respectively. Indeed, as the excitation amplitude increases, the differences decrease to 0.08 and 0.02. These differences are on the same magnitude as for the DEM. Although some quantitative differences between analytical formula and experimental results exist, the qualitative validity of the derived

formula is shown. Hence, the formulas for the optimal stroke Eq. (17) and dissipated energy Eq. (14) provide a powerful tool to support the design of a particle damper for an underlying structure.

Interestingly, the DEM simulations are in much better agreement with the analytical formula as the experiments. This might be attributable to the fact that some influence parameters affecting the experiments are neither reproduced by the analytical formula nor the DEM simulations. This will be further investigated in Sect. 6.

6 Sensitivity analysis

In order to obtain a deeper understanding of the influence parameters affecting the reduced loss factor, sensitivity analyses are performed on selected parameters in this section using the experimental setup and the numerical DEM model. First, different particle properties are studied in Sect. 6.1. Afterward, the influence of a container tilt is analyzed in Sect. 6.2. Finally, the effect of the container's shape is investigated in Sect. 6.3.

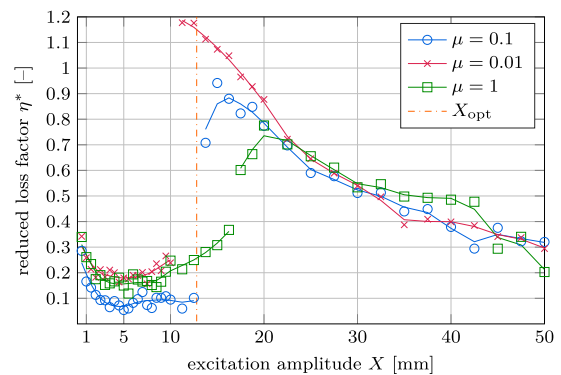
6.1 Particle properties

Using both, experiment and DEM, the effect of single particle properties on the reduced loss factor are investigated in the following. As only one property is varied at a time, independent results are obtained.

Young's modulus The Young's modulus of the particles is changed using the DEM to the values of PVC and tungsten, i.e., 3 and 405 GPa compared to 210 GPa of steel, using DEM simulations. Indeed, only minor differences of the reduced loss factor for 36 and 44 particles are obtained. Thus, the influence of the Young's modulus is negligible.

Density Likewise to the Young's modulus, the density values of PVC and tungsten are studied, i.e., 1400 kg/m³ and 19,250 kg/m³ compared to 7900 kg/m³ of steel, by DEM simulations. Again, only a negligible influence onto the reduced loss factor is obtained. However, it should be noted that the dissipated energy of the system is depending via Eq. (5) on the kinetic energy of the particles and thus on the particle mass as $E_{\text{diss}} = \eta^* E_{\text{kin}} = \eta^* \frac{1}{2} m_{\text{bed}} V^2$. Thus, using the particles density, the amount of dissipated energy can be influenced.

(a) 36 particles.



(b) 44 particles.

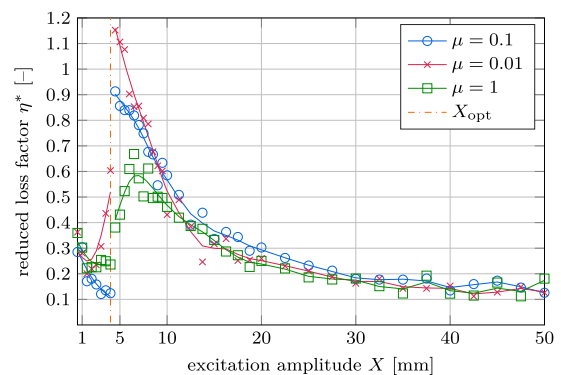


Fig. 6 Reduced loss factor of **a** 36 particles and **b** 44 particles for different friction coefficients analyzed by DEM. The threshold amplitude X_{opt} refers to Eq. (17)

Friction coefficient For the analysis of the friction coefficient, values of $\mu = 0.01$ and $\mu = 1$ are additionally analyzed by DEM and compared to the baseline simulation of $\mu = 0.1$. The results are shown for 36 and 44 particles in Fig. 6.

For both particle numbers, the same observations can be made. For low excitation amplitudes, i.e., the scattered state, only a little dependency on the friction coefficient is seen, which is not of higher importance.

At the optimal strokes, completely different results are obtained for the different friction coefficients. The higher the friction coefficient, the higher the optimal stroke, but the lower the maximum reduced loss factor. Differences up to a factor of 1.7 are seen in the reduced loss factor here, i.e., $\eta^* \approx 0.7$ for $\mu = 1$ to $\eta^* \approx 1.15$ for $\mu = 0.01$. This behavior can be explained, as a higher friction coefficient leads to more frictional energy dissipation. Hence, the particles' translational

velocity during impact with the opposite container wall is lower, leading to lower reduced loss factors. In addition, due to the lower translational velocity, the impact time point occurs later. Hence, the optimal stroke is shifted to higher values. For container strokes above the optimal strokes, the results of the different friction coefficients converge against each other, showing only minor differences. Thus, in these areas, the friction coefficient is of minor influence.

Using this knowledge, the differences in Fig. 4 between experimental results and DEM simulations with $\mu = 0.1$ might be explained. Especially, at the optimal strokes, the experiments lead to lower reduced loss factors, while for excitation amplitudes above the optimal strokes a convergence is observed. This behavior can partially be explained by an underestimation of the friction coefficient in the simulations.

Coefficient of restitution To investigate in the coefficient of restitution, instead of a velocity-dependent COR, three constant values of $\varepsilon = 0.8$, $\varepsilon = 0.9$, and $\varepsilon = 0.95$ are analyzed by DEM. One could expect a negative influence for high COR's, as instead of an inelastic collision particles might rebound from the impacting container wall for the rolling collect-and-collide motion mode. However, none of the values is showing a major influence on the reduced loss factor. Only for very high COR's $\varepsilon \rightarrow 1$, this might be the case [23]. However, as such a high value is not of practical importance, this is not further studied here.

Particle number and radius To analyze the effect of the particle number experimentally, these are stepwise reduced starting from 36 and 44 particles. By using a partition wall, the clearance is kept constant at $h = 3$ cm and $h = 1$ cm, respectively. No major influence on the reduced loss factor could be observed as long as more than three particles in length and width direction of the container are used. Only for a lower number of particle rows, the inelastic collision behavior of the particles is negatively influenced, which results in a lower reduced loss factor.

To analyze the effect of the particle radius experimentally, spheres of 2.5 mm radius instead of 5 mm radius are investigated. The particle number to cover the container base with one layer of particles changes to $N_{p,\max} = 192$. To keep the clearance at $h = 3$ cm and $h = 1$ cm, 144 and 176 particles, respectively, are utilized. From the analytical formula Eq. (14), no dependency on the particle radius is obtained. However, in the experiments, a much lower particle movement is

observed around the optimal strokes for the lower particle radius. This leads to much smaller reduced loss factors in this area. The other areas are only little affected. An explanation for this might be the highly increased surface area of the particles. Due to the strong influence of friction, as discussed earlier in this section, the lower particle movement might occur around the optimal stroke. Hence, bigger particles are beneficial. Also, for high excitation amplitudes, more particles take off the container base. This movement might already be classified as fluidization mode. However, further studies on this are above the scope of this paper.

It should be noted that the mass of the particle bed and thus the amount of dissipated energy can also be influenced by the number of particles and the particle radius. Thus, particle radius, particle number, and particle density should be considered during the design phase of the particle damper.

6.2 Tilt

In this section, an additional tilt around the three container axis, see Fig. 1, is analyzed. For high acceleration intensity applications, it is shown in [23] that such a tilt is not significantly affecting the dampers' energy dissipation. However, here the rolling property of spheres is used. This might lead to a different dependency on the container's tilt. In Fig. 7, the reduced loss factor is shown for an additional tilt α of 3° around the containers x -, y -, and z -axis for 36 and 44 particles using DEM simulations. The results are compared to the system with only a minor tilt of 0.1° , also called baseline setting in the following.

y-axis A tilt around the containers y -axis has only a minor influence on the reduced loss factor for both particle settings. It can thus be considered negligible.

z-axis A tilt around the z -axis is showing a major influence. For the 36 particle setting, the reduced loss factor is first close to $\eta^* \approx 0$ and thus, even lower as the baseline setting. When the container stroke reaches $X = 4$ mm, the reduced loss factor sharply increases and reaches values about $\eta^* \approx 0.5$. Around the optimal stroke, i.e., $X \approx X_{\text{opt},36}$, no sharp transition between scattered state and rolling collect-and-collide motion mode is seen. Here, much lower values compared to the baseline setting are obtained, i.e., values of about $\eta^* \approx 0.4$ compared to $\eta^* \approx 0.7$. At the highest reduced loss factor, this difference reduces with values of about

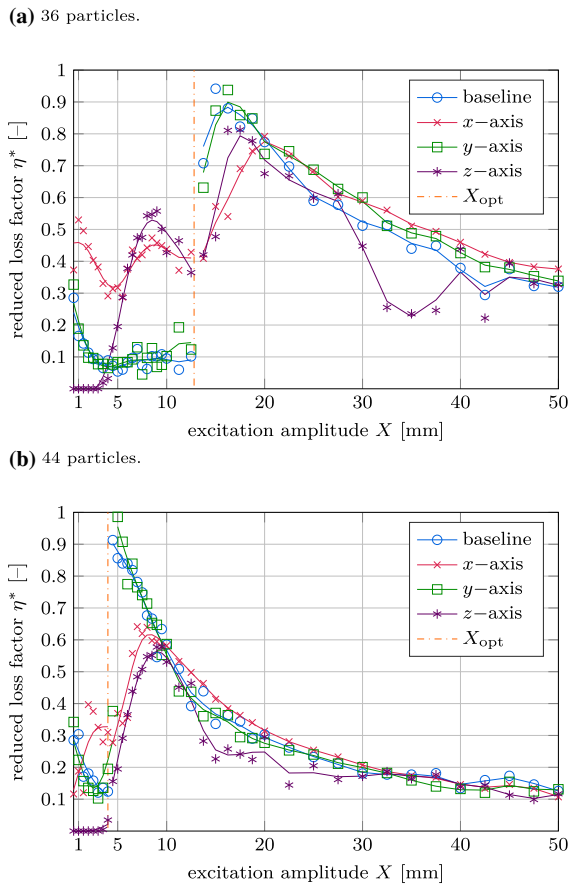


Fig. 7 Reduced loss factor of **a** 36 particles and **b** 44 particles for a container tilt of 3° around all its three axis by DEM simulations. The threshold amplitude X_{opt} refers to Eq. (17)

$\eta^* \approx 0.8$ and $\eta^* \approx 0.9$. For $X \gg X_{opt,36}$, the envelope of the reduced loss factor looks similar to the baseline setting.

For the 44 particle setting, the reduced loss factor is first also close to $\eta^* \approx 0$. When the container stroke reaches $X = X_{opt,44} = 4$ mm, the reduced loss factor increases up to $\eta^* \approx 0.55$. However, big differences to the baseline setting are seen around $X_{opt,44}$. For strokes above $X > 9$ mm, the envelope of the reduced loss factor is similar to the baseline setting.

To explain the observed behavior, the container's acceleration has to be considered. Due to the containers tilt, the particle bed will collect on the lower container wall for both motion modes. The particle bed can only leave the lower container wall if $A \cos(\alpha) > g \sin(\alpha)$ holds true. Hence, one obtains $A > 0.51 \text{ m/s}^2$. At the optimal strokes, the container accelerations follow for

36 particles to $A(X_{opt,36} = 12 \text{ mm}) = 1.9 \text{ m/s}^2$ and for 44 particles to $A(X_{opt,44} = 4 \text{ mm}) = 0.63 \text{ m/s}^2$.

Thus, for excitation amplitudes up to $X = 4$ mm the particles barely take off the lower container wall resulting in very low energy dissipation. Hence, only very low reduced loss factor values are seen for both particle numbers up to this container stroke. For higher container strokes, a new motion mode is observed. The particles leave the lower container wall, but they do not reach the other container side. Instead, single-sided contacts with the lower container wall are seen leading to reduced loss factors of about $\eta^* \approx 0.1 - 0.55$.

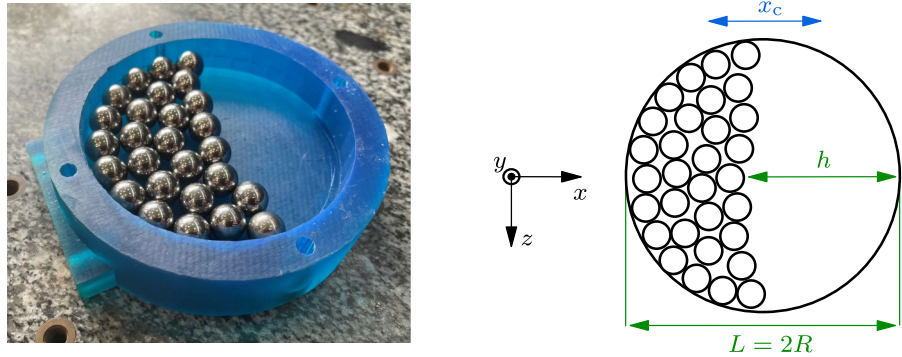
The rolling collect-and-collide motion mode occurs if the container acceleration gets high enough, such that the particle bed will reach the other container side. However, the maximum reduced loss factor is reduced in value and shifted to higher excitation strokes. Likewise, the higher the acceleration at the optimal stroke, the lower the influence due to the tilt. Hence, the reduced loss factor of the 36 particle setting is not as much affected as of the 44 particle setting.

For container strokes above the maximum reduced loss factor, the influence of the tilt becomes more and more negligible as the container acceleration increases. Thus, baseline setting and z -axis tilt look similar in this regime. In summary, to avoid a major influence of a container's z -axis tilt, one should make sure $A \cos(\alpha) \gg g \sin(\alpha)$ holds at the point of operation of the particle damper. This condition is hence the lower bound for the container acceleration and thus, for the container stroke and excitation frequency.

x -axis The envelope of the reduced loss factor looks very similar for a tilt around x - and z -axis for both particle numbers. Only for very small excitation amplitudes up to $X = 4$ mm, major differences are seen. Here, reduced loss factors between $\eta^* \approx 0.1 - 0.5$ instead of $\eta^* \approx 0$ are observed.

Although the envelope of the reduced loss factor looks similar for a tilt around x - and z -axis, different explanations are necessary. For a x -axis tilt, the particles get also collected at the lower container wall. Though, this is the sidewall now. Similar to the baseline setting, scattered and rolling collect-and-collide state are observed. For the scattered state, the x -axis tilt is advantageous compared to the baseline setting. As the particles get collected at the sidewall, more particle collisions occur, leading to higher energy dissipation. However, for the rolling collect-and-collide motion mode, the collection of particles hinder each

Fig. 8 Picture (left) and schematic representation (right) of cylinder



others movement. This results in lower reduced loss factors compared to the baseline setting. Only for high excitation amplitudes, the tilt's influence becomes negligible leading to similar reduced loss factors as the baseline setting.

Due to the similarity between x - and z -axis tilt, the same condition of $A \cos(\alpha) \gg g \sin(\alpha)$ should be considered during the dampers design phase. However, it is hard to derive this formula based on physical considerations for a x -axis tilt.

Comparing the simulation results for a tilt around x -axis or z -axis of Fig. 7 with the experimental results shown in Fig. 4, one observes a higher agreement compared to the baseline setting. Thus, besides an underestimation of the friction coefficient, a little tilt of the experimental setup around x -axis or z -axis might further explain the differences between experimental and numerical results.

6.3 Container shape

For the analyzed cuboid container, an excitation in the horizontal plane in the container's longitudinal direction is used until now. However, in some real technical applications, the excitation might occur in any direction in the horizontal plane, for instance for high-rise buildings or crane hooks. In this case, the clearance and thus, the optimal stroke and the reduced loss factor of a cuboid container would depend on the excitation direction, see Eqs. (6) and (17). To make the reduced loss factor independent of the excitation direction in the horizontal plane, a cylindrical container shape heading against gravity, i.e., in y -direction, see Fig. 8, is analyzed experimentally next. The cylinder has a radius of $R = 3.9$ cm. Thus, the same particle number of 48 is necessary to cover the container's base. Its height is

slightly above the particle's diameter with 11 mm. The clearance is approximated with Eq. (6) using $L = 2R$. To obtain the same clearances and thus, the same optimal strokes as for the cuboid container the particle numbers are reduced to 30 and 42.

In Fig. 9, the reduced loss factors are compared between experimentally obtained results of the cuboid and cylinder shape. Also, the reduced loss factor for a DEM simulation for the cylinder is shown.

Between the experimental results of cuboid and cylinder, only little differences occur in the reduced loss factor for both motion modes. Especially, for the rolling collect-and-collide of the 36 particle setting, slightly lower reduced loss factors are seen. For the DEM results, the same observations as for the cuboid DEM results, see Fig. 4, are obtained. The scattered state is only roughly approximated, while for the rolling collect-and-collide a good qualitative agreement with some quantitative discrepancies, especially around the optimal stroke, is achieved. In sum, the cylindrical container shape is well suited if the excitation direction in the horizontal plane is not well known. Also, the DEM model can be used for further sensitivity analysis.

Likewise, to the cuboid container shape, a tilt of 3° around the cylinders x - and z -axis, see Fig. 8, is analyzed by DEM simulations. From the results, shown in Fig. 10, the same statements as for a tilt of the cuboid of Fig. 7 can be drawn.

While for the scattered state, partially higher reduced loss factors are obtained, the optimal stroke of the rolling collect-and-collide is shifted slightly to higher values, but lower reduced loss factors are received. Likewise to the cuboid shape, the 42 particle setting is more influenced than the 30 particle setting. This happens as the container acceleration at the optimal stroke of the 42 particle setting is much lower compared to

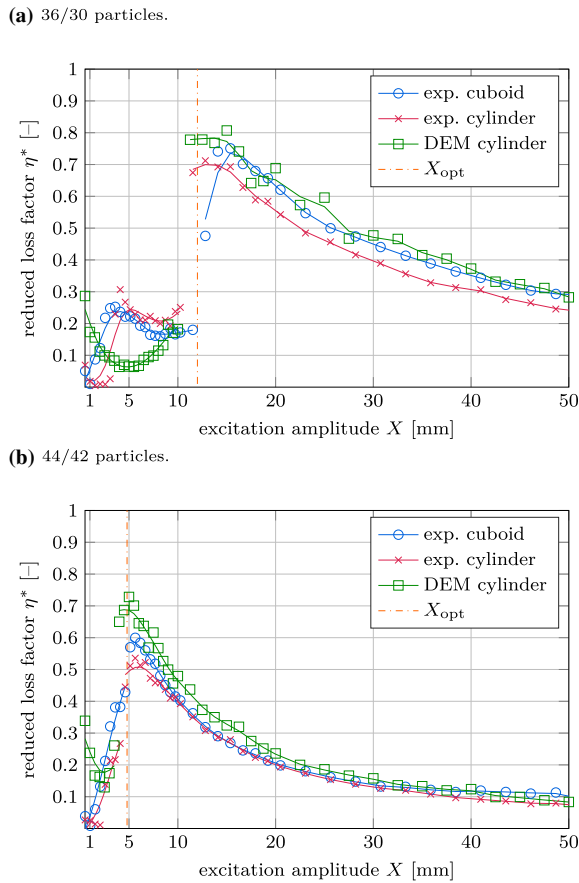


Fig. 9 Reduced loss factor of **a** 36 (cuboid) and 30 (cylinder) particles and **b** 44 (cuboid) and 42 (cylinder) particles. The threshold amplitude X_{opt} refers to Eq. (17)

the 30 particle setting, i.e., $A(X_{opt,30} = 12 \text{ mm}) = 1.9 \text{ m/s}^2$ to $A(X_{opt,44} = 4 \text{ mm}) = 0.63 \text{ m/s}^2$. Thus, the tilt of the container has more effect on the higher particle number due to the lower clearance. The results for a tilt around x - and z -axis are again only of minor differences. Likewise to the cuboid container shape, the condition of $A \cos(\alpha) \gg g \sin(\alpha)$ should be considered during the dampers design phase to avoid a large influence due to a tilt.

7 Conclusion

The attributes of particle dampers for low acceleration horizontal vibrations are analyzed. Using a linear drive a cuboid particle container is subjected to a harmonic motion. For low excitation amplitudes, a scattered state of the spherical particles is observed. No

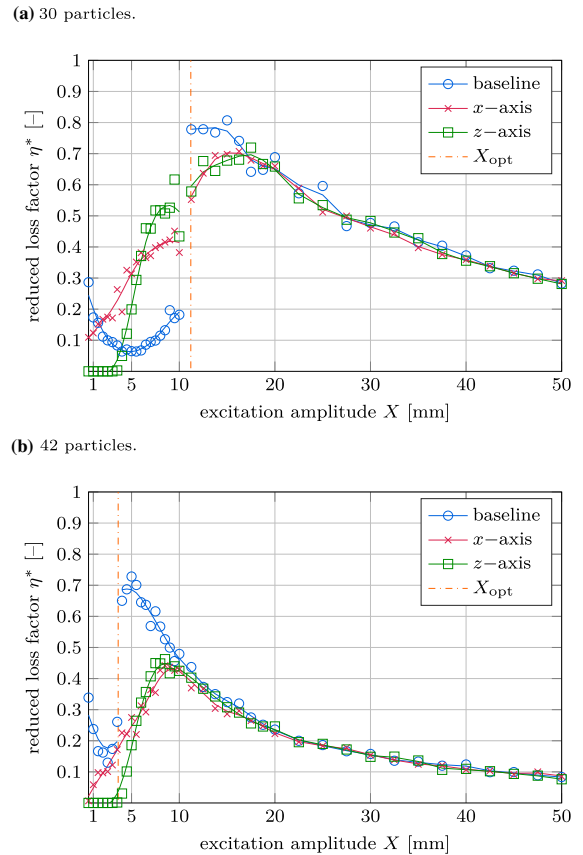


Fig. 10 Reduced loss factor of **a** 30 particles and **b** 42 particles for a cylindrical container with tilt of 3° around its x - and z -axis by DEM simulations. The threshold amplitude X_{opt} refers to Eq. (17)

regular movement is seen, and the damper's efficiency is low. If the excitation amplitude is exceeding a threshold amplitude, which only depends on the clearance of the particle bed to the opposite container wall, the system switches to the rolling collect-and-collide motion mode. Here, the particles slide and roll as one particle block over the container base and collide inelastically with the container's walls. This synchronous motion leads first to a high damper efficiency with a low reduction to higher container amplitudes.

While for the scattered state, an empirical formula is found to describe the energy dissipation, for the rolling collect-and-collide motion mode an analytical expression is derived. Especially, this analytical expression is in good agreement with the experimental measurements. Also, an analytical expression for the threshold

amplitude separating both motion modes is derived, fitting well to the measurements.

To obtain a deeper understanding of the dynamical processes inside the damper, experimental and numerical sensitivity analyses are performed. The numerical discrete element model is validated by comparisons to the conducted experiments, showing a good agreement. Most of the particle properties, like Young's modulus, density, coefficient of restitution, or particle number have a negligible influence on the damper's efficiency. However, it turns out that a low friction coefficient and a high particle radius are beneficial. Also, a tilt around the damper's axis are studied. Hereby, a little tilt around the dampers yaw axis is showing only little influence on the damper's efficiency. However, a tilt around its longitudinal or pitch axis might significantly decrease the efficiency of the rolling collect-and-collide motion mode. Finally, the container shape is analyzed experimentally and numerically. The cuboid shape is replaced by a cylindrical shape heading against gravity. While the efficiency of the damper is only a little reduced, this cylindrical shape is showing the great advantage of applying to vibrations in the whole horizontal plane. Thus, this new efficient damper design for low acceleration vibrations opens a completely new area of applications for particle dampers in mechanical and civil engineering.

Acknowledgements The authors would like to thank the German Research Foundation (DFG) for the financial support of the project 424825162. The authors would also like to thank Dr.-Ing. Marc-André Pick, Dipl.-Ing. Riza Demir, Dipl.-Ing. Norbert Borngräber-Sander and Wolfgang Brennecke for helping to design and realize the experimental rig.

Funding Open Access funding enabled and organized by Projekt DEAL. The project 424825162 is funded by the German Research Foundation (DFG).

Data availability The datasets generated during the current study are available from the corresponding author on reasonable request.

Declarations

Conflict of interest On behalf of all authors, the corresponding author states that there is no conflict of interest.

Ethical standard The authors state that this research complies with ethical standards. This research does not involve either human participants or animals.

Open Access This article is licensed under a Creative Commons Attribution 4.0 International License, which permits use, sharing, adaptation, distribution and reproduction in any medium or format, as long as you give appropriate credit to the original author(s) and the source, provide a link to the Creative Commons licence, and indicate if changes were made. The images or other third party material in this article are included in the article's Creative Commons licence, unless indicated otherwise in a credit line to the material. If material is not included in the article's Creative Commons licence and your intended use is not permitted by statutory regulation or exceeds the permitted use, you will need to obtain permission directly from the copyright holder. To view a copy of this licence, visit <http://creativecommons.org/licenses/by/4.0/>.

References

- Andersson, S., Söderberg, A., Björklund, S.: Friction models for sliding dry, boundary and mixed lubricated contacts. *Tribol. Int.* **40**(4), 580–587 (2007). <https://doi.org/10.1016/j.triboint.2005.11.014>
- Ansari, I.H., Alam, M.: Patterns and velocity field in vertically vibrated granular materials. *AIP Conf. Proc.* **1542**(1), 775–778 (2013). <https://doi.org/10.1063/1.4812046>
- Bannerman, M.N., Kollmer, J.E., Sack, A., Heckel, M., Mueller, P., Pöschel, T.: Movers and shakers: granular damping in microgravity. *Phys. Rev. E* **84** (2011). <https://doi.org/10.1103/PhysRevE.84.011301>
- Chen, J., Georgakis, C.T.: Tuned rolling-ball dampers for vibration control in wind turbines. *J. Sound Vib.* **332**(21), 5271–5282 (2013). <https://doi.org/10.1016/j.jsv.2013.05.019>
- Chen, T., Mao, K., Huang, X., Wang, M.: Dissipation mechanisms of nonobstructive particle damping using discrete element method. In: *Proceedings of SPIE—The International Society for Optical Engineering*, vol. 4331, pp. 294–301 (2001). <https://doi.org/10.1117/12.432713>
- Cundall, P.A., Strack, O.D.L.: A discrete numerical model for granular assemblies. *Int. J. Rock Mech. Min. Sci. Geomech.* **16**(4), 47–65 (1979). <https://doi.org/10.1680/geot.1979.29.1.47>
- Duan, Y., Chen, Q.: Simulation and experimental investigation on dissipative properties of particle dampers. *J. Vib. Control* **17**(5), 777–788 (2010). <https://doi.org/10.1177/1077546309356183>
- Eshuis, P., Weele, K., Meer, D., Lohse, D.: Granular leidenfrost effect: experiment and theory of floating particle clusters. *Phys. Rev. Lett.* **95** (2006). <https://doi.org/10.1103/PhysRevLett.95.258001>
- Gear, C.W.: The numerical integration of ordinary differential equations of various orders. *Math. Comput.* **21**(98), 146 (1967). <https://doi.org/10.2307/2004155>
- Gnanasambandham, C., Stender, M., Hoffmann, N., Eberhard, P.: Multi-scale dynamics of particle dampers using wavelets: extracting particle activity metrics from ring down experiments. *J. Sound Vib.* **454**, 1–13 (2019). <https://doi.org/10.1016/j.jsv.2019.04.009>

11. Gonthier, Y., McPhee, J., Lange, C., Piedbœuf, J.C.: A regularized contact model with asymmetric damping and dwell-time dependent friction. *Multibody Syst. Dyn.* **11**(3), 209–233 (2004). <https://doi.org/10.1023/B:MUBO.0000029392.21648.bc>
12. Hertz, H.: *The Principles of Mechanics: Presented in a New Form, Unabridged and Unaltered Republication of the 1 edn.* Dover books, Dover Publications, New York (1956)
13. Huang, X.H., Xu, W.B., Wang, J., Yan, W.M., Chen, Y.J.: Equivalent model of a multi-particle damper considering particle rolling and its analytical solution. *Struct. Control. Health Monit.* **28** (2021). <https://doi.org/10.1002/stc.2718>
14. Johnson, C.D.: Design of passive damping systems. *J. Mech. Des.* **117**(B), 171–176 (1995). <https://doi.org/10.1115/1.2838659>
15. Kollmer, J.E., Tupy, M., Heckel, M., Sack, A., Pöschel, T.: Absence of subharmonic response in vibrated granular systems under microgravity conditions. *Phys. Rev. Appl.* **3**(2), 024007 (2015). <https://doi.org/10.1103/PhysRevApplied.3.024007>
16. Lu, Z., Lu, X., Masri, S.: Studies of the performance of particle dampers under dynamic loads. *J. Sound Vib.* **329**, 5415–5433 (2010). <https://doi.org/10.1016/j.jsv.2010.06.027>
17. Lu, Z., Wang, D., Masri, S., Lu, X.: An experimental study of vibration control of wind-excited high-rise buildings using particle tuned mass dampers. *Smart Struct. Syst.* **18**, 93–115 (2016). <https://doi.org/10.12989/sss.2016.18.1.093>
18. Masmoudi, M., Job, S., Abbes, M.S., Tawfiq, I., Haddar, M.: Experimental and numerical investigations of dissipation mechanisms in particle dampers. *Granular Matter* **18**(3), 71 (2016). <https://doi.org/10.1007/s10035-016-0667-4>
19. Matchett, A.J., Yanagida, T., Okudaira, Y., Kobayashi, S.: Vibrating powder beds: a comparison of experimental and distinct element method simulated data. *Powder Technol.* **107**(1), 13–30 (2000). [https://doi.org/10.1016/S0032-5910\(99\)00080-7](https://doi.org/10.1016/S0032-5910(99)00080-7)
20. Mcnamara, S., Young, W.R.: Inelastic collapse and clumping in a one-dimensional granular medium. *Phys. Fluids A* **4**(3), 496–504 (1992). <https://doi.org/10.1063/1.858323>
21. Mehta, A., Luck, J.M.: Novel temporal behavior of a nonlinear dynamical system: the completely inelastic bouncing ball. *Phys. Rev. Lett.* **65**(4), 393–396 (1990). <https://doi.org/10.1103/PhysRevLett.65.393>
22. Meyer, N., Seifried, R.: Numerical and experimental investigations in the damping behavior of particle dampers attached to a vibrating structure. *Comput. Struct.* **238** (2020). <https://doi.org/10.1016/j.compstruc.2020.106281>
23. Meyer, N., Seifried, R.: Toward a design methodology for particle dampers by analyzing their energy dissipation. *Comput. Part. Mech.* **8**(4), 681–699 (2021). <https://doi.org/10.1007/s40571-020-00363-0>
24. Meyer, N., Schwartz, C., Morlock, M., Seifried, R.: Systematic design of particle dampers for horizontal vibrations with application to a lightweight manipulator. *J. Sound Vib.* **510**, 116319 (2021). <https://doi.org/10.1016/j.jsv.2021.116319>
25. Morlock, M., Meyer, N., Pick, M.A., Seifried, R.: Modeling and trajectory tracking control of a new parallel flexible link robot. In: *Proceedings of the 2018 IEEE/RSJ International Conference on Intelligent Robots and Systems (2018)*. <https://doi.org/10.1109/IROS.2018.8594008>
26. Morlock, M., Meyer, N., Pick, M.A., Seifried, R.: Real-time trajectory tracking control of a parallel robot with flexible links. *Mech. Mach. Theory* **158**, 104220 (2021). <https://doi.org/10.1016/j.mechmachtheory.2020.104220>
27. Panossian, H.: Structural damping enhancement via non-obstructive particle damping technique. *J. Vib. Acoust.* **105**(114), 101–105 (1992). <https://doi.org/10.1115/1.2930221>
28. Panossian, H.: Non-obstructive particle damping experience and capabilities. In: *Proceedings of SPIE—The International Society for Optical Engineering*, vol. 4753, pp. 936–941 (2002). <https://doi.org/10.2514/6.2008-2102>
29. Pöschel, T.: *Computational Granular Dynamics: Models and Algorithms.* Springer, Berlin (2005). <https://doi.org/10.1007/3-540-27720-X>
30. Sack, A., Heckel, M., Kollmer, J., Zimmer, F., Pöschel, T.: Energy dissipation in driven granular matter in the absence of gravity. *Phys. Rev. Lett.* **111** (2013). <https://doi.org/10.1103/PhysRevLett.111.018001>
31. Saluena, C., Esipov, S.E., Poeschel, T., Simonian, S.S.: Dissipative properties of granular ensembles. *Proc. SPIE* **3327**(1), 23–29 (1998). <https://doi.org/10.1117/12.310696>
32. Sanchez, M., Rosenthal, G., Pugnali, L.: Universal response of optimal granular damping devices. *J. Sound Vib.* **331**(20), 4389–4394 (2012). <https://doi.org/10.1016/j.jsv.2012.05.001>
33. Simonian, S.S.: Particle beam damper. In: *Proceedings of SPIE—The International Society for Optical Engineering*, vol. 2445, pp. 149–160 (1995). <https://doi.org/10.1117/12.208884>
34. Wong, C.X., Daniel, M.C., Rongong, J.A.: Energy dissipation prediction of particle dampers. *J. Sound Vib.* **319**(1–2), 91–118 (2009). <https://doi.org/10.1016/j.jsv.2008.06.027>
35. Yang, M.Y., Lesieutre, G.A., Hambric, S., Koopmann, G.: Development of a design curve for particle impact dampers. *Noise Control Eng. J.* **53**, 5–13 (2005). <https://doi.org/10.1117/12.540019>
36. Yin, Z., Su, F., Zhang, H.: Investigation of the energy dissipation of different rheology behaviors in a non-obstructive particle damper. *Powder Technol.* **321** (2017). <https://doi.org/10.1016/j.powtec.2017.07.090>
37. Zhang, K., Chen, T., Wang, X., Fang, J.: Rheology behavior and optimal damping effect of granular particles in a non-obstructive particle damper. *J. Sound Vib.* **364** (2015). <https://doi.org/10.1016/j.jsv.2015.11.006>
38. Zhang, K., Chen, T., He, L.: Damping behaviors of granular particles in a vertically vibrated closed container. *Powder Technol.* **321**, 173–179 (2017). <https://doi.org/10.1016/j.powtec.2017.08.020>

Publisher's Note Springer Nature remains neutral with regard to jurisdictional claims in published maps and institutional affiliations.